



Aerosol-assisted flow synthesis of B-doped, Ni-doped and B–Ni-codoped TiO₂ solid and hollow microspheres for photocatalytic removal of NO

Yu Huang^a, Wingkei Ho^b, Zhihui Ai^a, Xiao Song^a, Lizhi Zhang^{a,*}, Shuncheng Lee^{b,*}

^a Key Laboratory of Pesticide & Chemical Biology of Ministry of Education, College of Chemistry, Central China Normal University, Luoyu Road No. 152, Wuhan 430079, Hubei, People's Republic of China

^b Department of Civil and Structural Engineering, Research Center for Environmental Technology and Management, The Hong Kong Polytechnic University, Hong Kong, China

ARTICLE INFO

Article history:

Received 19 July 2008

Received in revised form 17 December 2008

Accepted 19 December 2008

Available online 30 December 2008

Keywords:

TiO₂

Photocatalysis

Doped

NO removal

Ni

B

Aerosol-assisted flow synthesis

ABSTRACT

In this study, highly effective B-doped, Ni-doped and B–Ni-codoped TiO₂ microspheres photocatalysts were directly synthesized via an aerosol-assisted flow synthesis method. The resulting samples were characterized by XRD, SEM, TEM, UV–vis diffuse reflectance spectroscopy, nitrogen adsorption and XPS. The characterizations revealed hollow microspherical structure of the B-doped and B–Ni-codoped TiO₂ photocatalysts, while the Ni-doped and undoped TiO₂ products consisted of solid microspheres. It was found that the boron dopant was partially embedded into the interstitial TiO₂ structure, existing in the form of Ti–O–B structure. The band gap was enlarged after the boron doping. However, both Ni-doped and B–Ni-codoped TiO₂ samples showed obvious red shift in their absorption edges because of the Ni doping. The photocatalytic activities of these samples were evaluated on the photocatalytic removal of NO under simulated solar light irradiation. All the aerosol-assisted flow synthesized samples had much higher photocatalytic activities than P25 and the doped TiO₂ microspheres exhibited enhanced photocatalytic activity than the undoped counterparts. More interestingly, the B–Ni-codoped TiO₂ photocatalyst possessed superior photocatalytic activity to the as-prepared single doped TiO₂ products. The enhanced photocatalytic activity was explained and the formation mechanisms of hollow and solid microspheres were also proposed on the basis of characterizations. We think this general method may be easily scaled up for industrial production of highly active microspherical photocatalysts for efficient NO removal under simulated solar light irradiation.

© 2008 Elsevier B.V. All rights reserved.

1. Introduction

The indoor air quality (IAQ) has attracted more and more attentions in recent years [1]. Nitrogen oxide is one of the most common gaseous pollutants found in the indoor environment with the concentration in the range of 70–500 parts-per-billion (ppb) levels [2]. Photocatalysis technique provides a very promising solution for the removal of indoor air pollutants at low concentration [3,4]. TiO₂, as the most promising photocatalyst, has been widely studied for air purification due to its nontoxicity, strong oxidation power and chemical inertness. However, it only absorbs wavelength in the near UV region ($\lambda < 400$ nm) for activation. As the visible light constitutes 95% of indoor light and 43% of solar light [5], it is meaningful to extend the optical absorption of TiO₂ from UV to visible light region for the effective use of solar energy and application of photocatalysts to indoor environments.

Enhancing the TiO₂ photocatalytic activity under visible or solar light is still a significant issue. Recently, doping TiO₂ with nonmetals has received much attention [6,7]. For instance, N [8,9], C [10,11], S [12,13], P [14,15], F [16], and I-doped [17,18] TiO₂ catalysts have been reported in the literatures. Compared with these nonmetals, doping boron has been much less studied [19,20] and the corresponding literature was controversial. The study of Grey et al. [20] suggested that partial reduction of Ti⁴⁺ to Ti³⁺ would be induced when boron was incorporated into rutile TiO₂, resulting in the high photocatalytic activity. In 2004, Zhao et al. [19] reported on doped TiO₂ with both boron and Ni₂O₃ by a modified sol–gel method. Their findings displayed that the incorporation of boron into TiO₂ lattice can efficiently extend the spectral response to the visible light region which was also found by other researchers [9,21]. Most recently, B–N-codoped TiO₂ were successfully fabricated by Lambert and co-workers [22] via a reproducible method. The boron modified products showed apparent absorption in the visible light region exhibiting improved photocatalytic activity under visible light irradiation. Cheng and co-workers used a simple strategy to obtain B/N-doped titania with a greatly enhanced visible-light absorption and showed that

* Corresponding authors. Tel.: +86 27 6786 7535; fax: +86 27 6786 7535.
E-mail addresses: zhanglz@mail.ccnu.edu.cn (L. Zhang), ceslee@polyu.edu.hk (S. Lee).

the visible-light activity of B-doped titania can be substantially enhanced by the formation of a B–N structure on the surface of titania [23]. On the contrary, Jiang and co-workers [24] found that the band gap of B-doped TiO_2 increased which was attributed to the decrease of the crystal size after boron doping. The blue shift phenomenon in the UV–vis spectrum was also observed in the study of B_2O_3 – SiO_2 /TiO₂ ternary mixed oxides when the boron content was less than 5% [21].

Because of the high surface area, large light-harvesting capacity and high energy conversion efficiency, hollow structured TiO₂ materials have drawn considerable attention in recent years [25,26]. Various methods such as hydrothermal method [27,28] and electrospraying method [29] have been developed to fabricate TiO₂ photocatalysts with hollow structure. The template approach (e.g. polymerization/sol–gel process [30] and layer-by-layer self-assembly technique [31]) was also adopted to obtain hollow structured titania. However, this technique requires subsequent removal of the sacrificial templates by calcination or chemical etching. Aerosol-assisted flow synthesis method is convenient and simple, which is a green versatile technique suitable for the synthesis of a variety of inorganic and organic materials [32,33]. A distinctive feature of the resulting sample obtained via the aerosol-assisted flow synthesis method is the homogeneous distribution of constituents throughout all of the particles because all of the constituents are formed from a solution. For example, in our previous work, we successfully prepared a series of $\text{Ti}_{1-x}\text{Zr}_x\text{O}_2$ ($x = 0.00, 0.045, 0.090, 0.135$, and 0.180) solid solutions photocatalysts in one step with this method [34]. The as-prepared solid solutions were microspheres with core-shell structures and exhibited high photocatalytic activity on the degradation of rhodamine B (RhB) in aqueous solution under simulated solar light irradiation consisting of both ultraviolet and visible light.

In the present work, B-doped, Ni-doped and B–Ni-codoped TiO₂ microsphere photocatalysts with enhanced photocatalytic activity on NO removal were obtained directly via an aerosol-assisted flow synthesis method. The resulting photocatalysts were investigated using XRD, SEM, and TEM, nitrogen adsorption, XPS and UV–vis spectroscopy. The synergistic effect of boron and nickel codoping on the intrinsic characteristics of TiO₂ was also investigated.

2. Experimental

2.1. Synthesis of B-doped, Ni-doped and B–Ni-codoped TiO₂ photocatalysts

B-doped, Ni-doped and B–Ni-codoped TiO₂ photocatalysts were prepared by an aerosol-assisted flow synthesis method. For the synthesis of B-doped TiO₂, TiCl_4 (10 mmol) and H_3BO_3 (10 mmol) were added to 100 mL of distilled water at 4 °C under vigorous stirring. The solution was nebulized at $1.7 \text{ MHz} \pm 10\%$ (YUYUE402AI, Shanghai) and then carried by air flow through a quartz tube surrounded by a furnace thermostated at 600 °C for about one and a half hour. The quartz reaction tube with the diameter of 3.5 cm was 1 m long. The products were collected in a percolator with distilled water, then separated by centrifugation, washed thoroughly with ethanol and distilled water, and finally dried in an oven at 50 °C. Ni-doped TiO₂ was obtained via the same method with $\text{NiCl}_2 \cdot 2\text{H}_2\text{O}$ (1 mmol) and TiCl_4 (10 mmol) as precursors. Under the same conditions, B–Ni-codoped TiO₂ was synthesized with the existence of $\text{NiCl}_2 \cdot 2\text{H}_2\text{O}$ (1 mmol), H_3BO_3 (10 mmol) and TiCl_4 (10 mmol) in the precursor solution. For comparison, undoped TiO₂ (pure TiO₂) was synthesized without the addition of H_3BO_3 or $\text{NiCl}_2 \cdot 2\text{H}_2\text{O}$ into the precursor solution under the same conditions.

Undoped TiO₂ (pure TiO₂), B-doped TiO₂, Ni-doped TiO₂ and B–Ni-codoped TiO₂ were designated as PT, BT, NT and BNT, respectively.

2.2. Characterization

The X-ray diffraction (XRD) patterns were recorded on a Bruker D8 Advance X-ray diffractometer with $\text{Cu K}\alpha$ radiation ($\lambda = 1.54178 \text{ \AA}$) at a scan rate of $0.05^\circ 2\theta/\text{s}$. The accelerating voltage and the applied current were 40 kV and 40 mA, respectively. Scanning electron microscopy (SEM, JSM-5600) was used to characterize the morphology of the obtained products. Transmission electron microscopy (TEM) study was carried out on a Philips CM-120 electron microscopy instrument. The samples for TEM were prepared by dispersing the final powders in methanol; the dispersion was then dropped on carbon copper grids. The nitrogen adsorption and desorption isotherm at -196°C was measured using a Micromeritics ASAP2010 system after sample being vacuum-dried at 200 °C overnight. A Varian Cary 100 Scan UV–Visible system equipped with a Labsphere diffuse reflectance accessory was used to obtain the reflectance spectra of the catalysts over a range of 200–800 nm. Labsphere USRS-99-010 was employed as a reflectance standard. The spectra were converted from reflection to absorbance by Kubelka–Munk method. X-ray photoelectron spectroscopy (XPS) measurements were performed on a PHI Quantum 2000 XPS System with a monochromatic Al $\text{K}\alpha$ source and a charge neutralizer. All the binding energies were calibrated to the C 1s peak at 284.8 eV of the surface adventitious carbon.

2.3. NO removal test

The NO removal with the resulting samples was performed at ambient temperature in a continuous flow reactor. The volume of the rectangular reactor which was made of stainless steel and covered with Saint-Glass was 27.3 L (13 cm (H) \times 70 cm (L) \times 30 cm (W)). Three sample dishes containing the photocatalysts powders were placed on a single path in the reactor. A 300-W commercial tungsten halogen lamp (General Electric) was used as the simulated solar light source. The integrated UV intensity in the range 310–400 nm is $720 \pm 10 \text{ W/cm}^2$. The lamp was vertically placed outside the reactor above the three sample dishes. Four mini fans were fixed around the lamp to avoid the temperature rise of the flow system. Furthermore, adequate distance was also kept from the lamp to the reactor for the same purpose to avoid temperature rise.

For activity test, the sample was prepared by coating an aqueous suspension of the photocatalyst onto three dishes with a diameter of 5.0 cm. The weight of the photocatalysts used for each experiment was kept at 0.3 g. The dishes containing the photocatalyst were pretreated at 70 °C for several hours until a complete removal of water in the suspension and then cooled to room temperature before use.

The NO gas was photocatalytically removed at ambient temperature. The NO gas was acquired from compressed gas cylinder at a concentration of 48 ppm NO (N_2 balance, BOC gas) with traceable National Institute of Standards and Technology (NIST) standard. The initial concentration of NO was diluted to about 400 ppb by the air stream supplied by a zero air generator (Thermo Environmental Inc. Model 111). The desired humidity level of the NO flow was controlled at 70% (2100 ppmv) by passing the zero air streams through a humidification chamber. The gas streams were pre-mixed completely by a gas blender and the flow rate was controlled at 4 L min^{-1} by a mass flow controller. After the adsorption–desorption equilibrium among water vapor, gases and photocatalysts was achieved, the lamp was turned on. The concentration of NO was continuously measured by a chemiluminescence NO analyzer (Thermo Environmental Instruments Inc. Model 42c), which monitors NO, NO₂, and NO_x (NO_x represents NO + NO₂) with a sampling rate of 0.7 L min^{-1} . The reaction of NO with air was ignorable when performing a control experiment with or without light in the absence of photocatalyst.

3. Results and discussion

3.1. XRD analysis

Fig. 1 shows the X-ray diffraction (XRD) patterns of the as-prepared products. All the peaks can be perfectly indexed as anatase phase of TiO_2 (JCPDS, file no. 84-1285, Space Group: $I4_1/amd$ (1 4 1)) for all the samples. The peak intensity of NT and BNT was not as intense as that of PT and BT, as observed from Fig. 1. This indicates relatively lower crystallinity of NT and BNT compared to PT and BT. The average crystalline sizes estimated from the (1 0 1) peaks were 9.8, 10.9, 7.4 and 7.2 nm for the samples of PT, BT, NT and BNT, respectively. Compared with that of undoped TiO_2 sample (PT), the crystalline size of TiO_2 increased after boron doping (BT), consistent with the literature [21]. In contrast, the anatase grain size decreased significantly with nickel doping. This decrease in crystallite size probably arises from the introduction of Ni^{2+} ions, which changed the surface charge of the TiO_2 sol particles and distanced them from each other during the synthesis process [35]. The size of BNT showed no distinct discrepancy with that of NT.

3.2. SEM images

Fig. 2 shows SEM images of the as-prepared samples. Both PT (Fig. 2a) and NT (Fig. 2d) consisted of solid microspheres with relatively smooth surface. Their diameters were in the range of several hundred nanometers to several micrometers. Interestingly, after the addition of boron dopant, the microstructure of the microspheres changed significantly. Hollow structured micro-

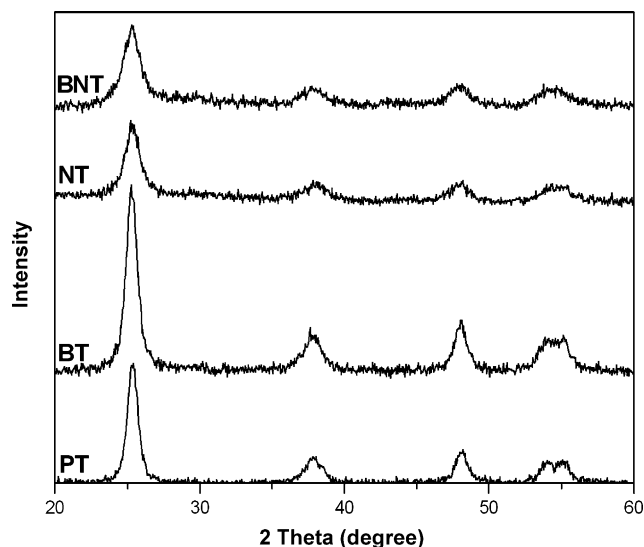


Fig. 1. XRD patterns of the undoped (PT), B-doped (BT), Ni-doped (NT) and B–Ni-codoped TiO_2 (BNT) products synthesized with the aerosol-assisted flow synthesis method.

spheres could be observed in both BNT and BT samples (Fig. 2b and c). The appearance of hollow structures could be ascribed to the escape of gas phase HBO_2 from the inner part of the TiO_2 microspheres during the pyrolysis reaction, which will be discussed in detail later. Their overall morphologies and sizes were similar to those of PT and NT products. As shown in Fig. 2c,

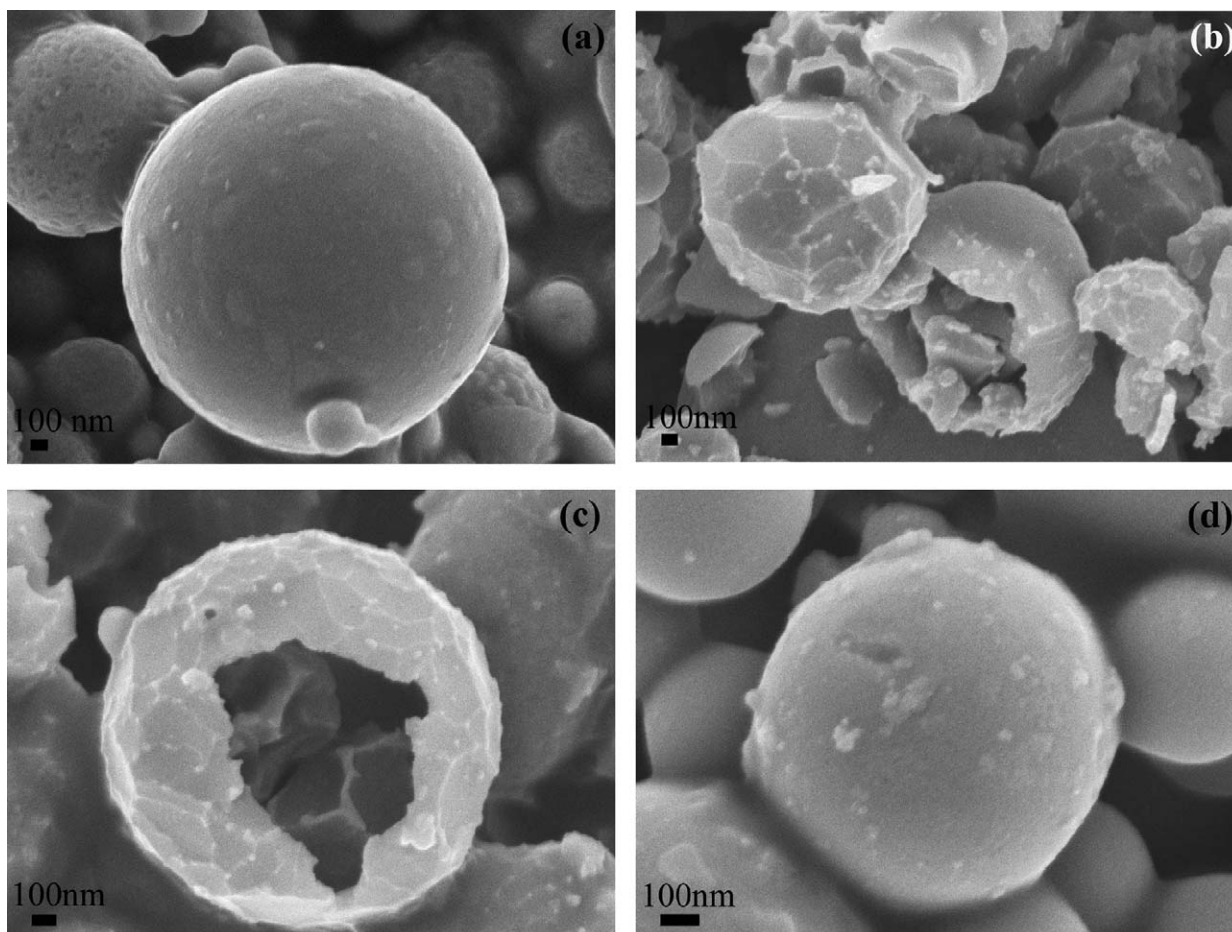


Fig. 2. SEM images of the resulting photocatalysts synthesized with the aerosol-assisted flow synthesis method. (a) PT, (b) BNT, (c) BT and (d) NT.

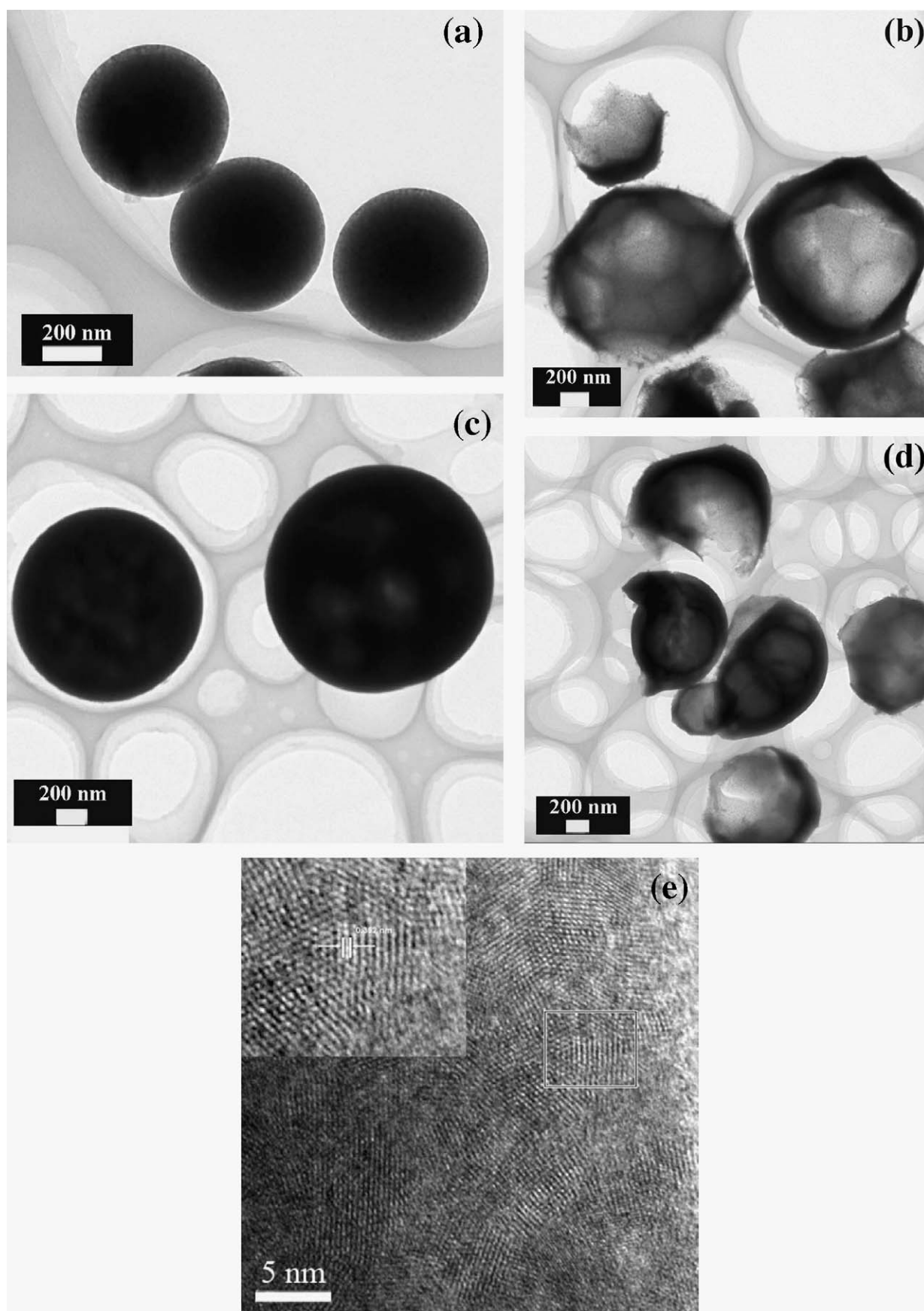


Fig. 3. TEM and HRTEM images of the resulting photocatalysts. (a) PT, (b) BT, (c) NT, (d) BNT and (e) HRTEM images of BNT.

the BT powders predominantly consisted of hollow structured microspheres with 1–2 μm in diameter. The shell was very thin and therefore we can observe some obvious shrinkage on the surface of sample BT. The shell thickness of the sample BNT was thicker than that of BT particles probably because of the existence of nickel oxide in the resulting sample.

3.3. TEM images

The size and morphology of the resulting products obtained from the aerosol-assisted flow synthesis method were further analyzed by TEM and HRTEM image. As shown in the TEM images in Fig. 3, only the BT and BNT samples consisted of hollow structured spheres, confirming the SEM results. The hollow structure was not found in PT and NT products (Fig. 3a and c). This indicates the doping of boron was crucial for the formation of hollow structure. From Fig. 3b, we can clearly see some stripes on the surface of BT product resulting from the shrinkage of the thin shell, while this phenomenon is not so obvious for the sample BNT (Fig. 3d). Furthermore, the lattice spacing is about 3.52 Å between adjacent lattice planes of the BNT product (HRTEM image, Fig. 3e), corresponding to the distance between (1 0 1) crystal planes of the anatase phase.

3.4. Nitrogen sorption

The N_2 adsorption–desorption isotherms and pore size distribution curves of the resulting photocatalyst samples are shown in Fig. 4. The pore size distribution was calculated from the desorption branch of nitrogen isotherms by Barret–Joyner–Halenda (BJH) method using the Halsey equation. In Fig. 4a, the physioadsorption isotherms can be classified as type IV with hysteresis loops in the IUPAC classification [36]. The pore size distributions of the resulting samples showed considerable difference as displayed in Fig. 4b. The pore size distribution of BT was broader than that of other products. Accompanying with the coexistence of Ni and B dopants in TiO_2 , the intensity of the pore size distribution decreased slightly. The Brunauer–Emmett–Teller (BET) specific surface areas and pore volumes of PT, BT, NT and BNT were summarized in Table 1. The hollow structured BT sample possessed the highest surface area (106 m^2/g), three times of that of PT powders (39 m^2/g). However, with the coexistence of Ni and B in TiO_2 , the surface area decreased to 90 m^2/g . It was reported that the increase of both the surface area and the crystallinity was promised to enhance the photocatalytic activity [37]. The crystalline size of the BT powders increased significantly comparing with that of PT, as shown by the XRD patterns in Fig. 1. The higher crystallinity could reduce the bulk defects, while the high surface area can probably facilitate the mass transfer of reactants (NO) or reaction intermediates. Therefore, it is expected that the high surface area and high crystallinity of our products could enhance the photocatalytic activity.

3.5. UV–vis diffuse reflectance spectra

The UV–vis diffuse reflectance spectra (DRS) of the samples are shown in Fig. 5. Strong absorption in the ultraviolet region ascribed to the band–band transition can be observed clearly for all the samples. The absorption edge of BT sample moved toward shorter wavelength in comparison with that of PT, indicating the band gap was enlarged after boron doping. It is commonly accepted that a larger band gap corresponds to a more powerful redox ability [38]. However, for the samples NT and BNT, the absorption edge shifted obviously to the visible light region mainly because the energy level for $\text{Ni}^{2+}/\text{Ni}^+$ lies below the conduction band edge and above the valence band edge of TiO_2 [35]. Assuming the material to be

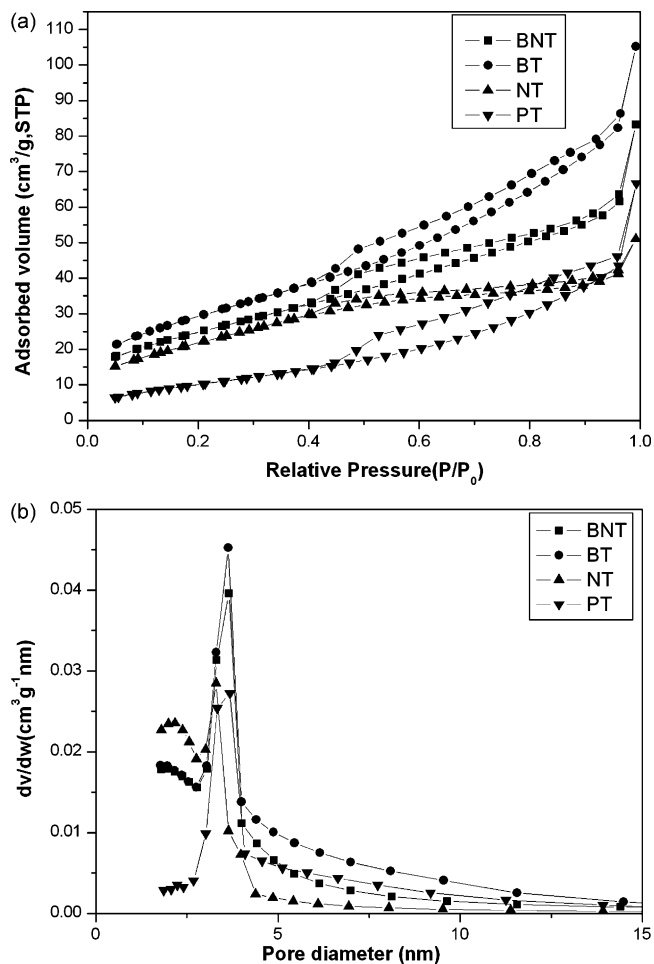


Fig. 4. (a) N_2 adsorption–desorption isotherms and (b) Barret–Joyner–Halenda (BJH) pore size distribution plot of the resulting photocatalyst samples.

indirect semiconductors, the band gap energies of PT, BT, NT and BNT calculated by the transformed Kubelka–Munk function were 2.78, 2.98, 1.94 and 2.25 eV, respectively.

3.6. XPS spectra

X-ray photoelectron spectroscopy was used to investigate the chemical compositions of the resulting products. Fig. 6 shows the high resolution spectra of B 1s (a), Ti 2p (b) and Ni 2p (c). In Fig. 6a, the B 1s emission shows peak with the binding energy at 191.9 eV in BNT sample. Peaks at 187.5 eV corresponding to B–Ti bond in TiB_2 were not found in our sample. As reported by Lambert and co-workers [22], low BE peak at 190.6 eV corresponds to boron actually incorporated into the TiO_2 lattice through occupying O sites, thereby inducing the unprecedented visible light photocatalytic activity of B-doped TiO_2 . However this peak did not appear in the B 1s spectra either. Therefore, it was inferred that the peak at 191.9 eV corresponding to boron which was probably

Table 1
Summary of the physicochemical properties of the resulting catalysts.

Materials	A_{BET} (m^2/g)	V_{BH} (cm^3/g)	Pore diameter (nm)
PT	39	0.11	7.3
BT	106	0.16	5.6
NT	78	0.08	3.8
BNT	90	0.13	5.4

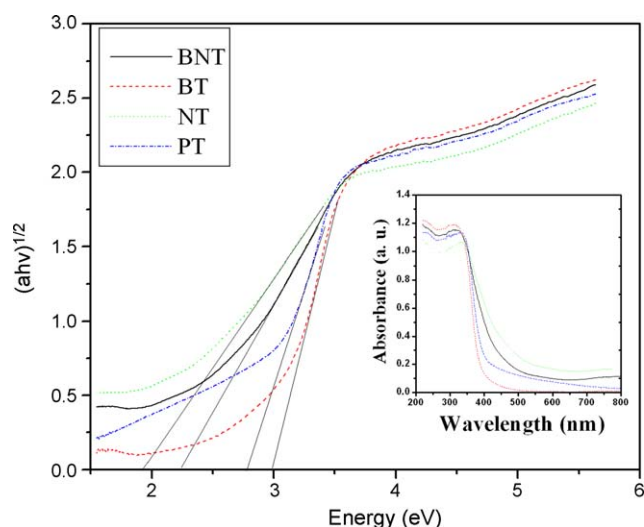


Fig. 5. Diffuse reflectance absorption spectra of the as-prepared samples. Data are plotted as transformed Kubelka–Munk function versus the energy of light. Insert shows the absorption spectra between 200 and 800 nm.

woven into the interstitial TiO_2 structure, existing in the form of Ti–O–B structure, which was consistent with the result reported by Jiang and co-workers [24]. Based on the XPS spectra, the B concentration in sample BNT was 0.99 at.%. As shown in Fig. 6b, the peaks of Ti $2p_{3/2}$ in all the resulting samples appeared around 459 eV, indicating that Ti ions are in an octahedral environment. It is observed that the binding energy of the Ti $2p_{3/2}$ peaks for BT, NT and BNT has an obvious chemical shift to a lower binding energy compared with that of PT, indicating a decrease of effective positive charge of Ti. The XPS analysis also showed the presence of Ni for the NT and BNT samples in Fig. 6c. The binding energy at 855.5 eV was assigned to NiO [39]. No evidence of other oxidation states of nickel was found. The nickel concentrations were 0.83 and 0.7 at.% in sample NT and BNT based on the XPS analysis, respectively.

3.7. Photocatalytic NO removal activities

Fig. 7 shows the relative variations of the NO removal rate against irradiation time in the presence of PT, BT, NT, BNT, and Degussa P25 under simulated solar light irradiation at a single pass flow through the reactor under a humidity level of 2100 ppmv. Prior to the simulated solar light irradiation, the adsorption/desorption equilibrium between the indoor air with NO and photocatalysts had been reached. When the solar light lamp was switched on, the photocatalytic degradation reaction of NO was initiated. It was found that the photolysis of NO without photocatalysts was negligible under simulated solar light irradiation. As shown in Fig. 7, the removal rate of both boron doped samples reached the highest value of 58 and 53 ppb/min for BNT and BT, respectively only after 30 min under simulated solar light irradiation. The NT showed a lower removal rate which was 47 ppb/min after being irradiated for 40 min. Without any doping, pure TiO_2 only exhibited a low removal rate of 15 ppb/min. In contrast, the famous commercial photocatalyst Degussa P25 showed very poor activity on NO removal under simulated solar light irradiation. Therefore, all the aerosol-assisted flow synthesized samples had much higher photocatalytic activities than P25 and the doped TiO_2 microspheres exhibited enhanced photocatalytic activity than the undoped counterparts. More interestingly, the B–Ni-codoped TiO_2 photocatalyst possessed superior photocatalytic activity to the as-prepared B- and Ni-doped TiO_2 products. According to our previous study [40], reactive oxygen

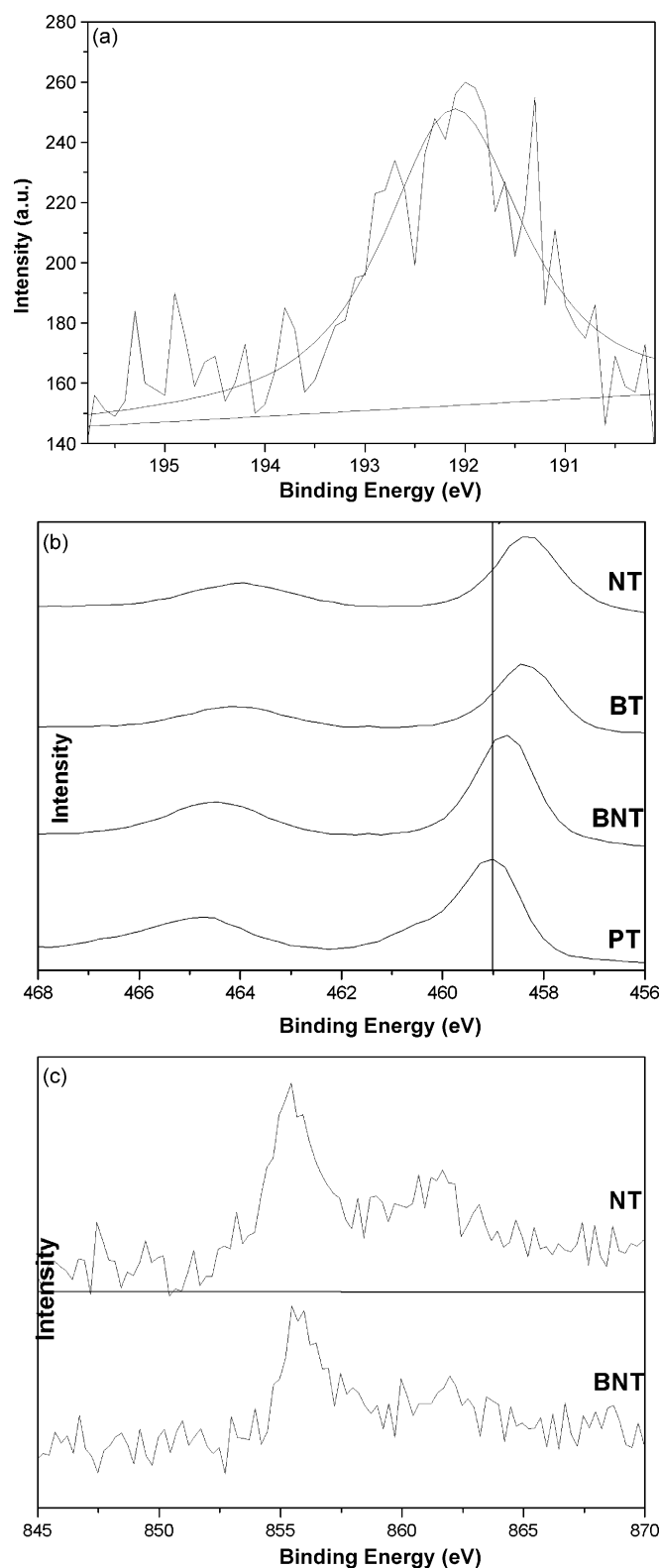
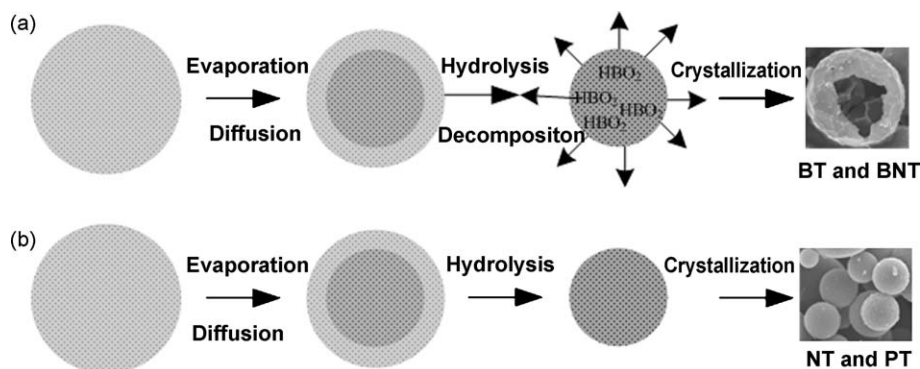


Fig. 6. XPS spectra of the resulting samples: (a) high resolution XPS spectra for B 1s of the sample B- and Ni-codoped TiO_2 ; (b) high resolution XPS spectra of Ti 2p for all the resulting samples; (c) high resolution XPS spectra of Ni 2p for BNT and NT samples.

species such as super oxide (O_2^-) and hydroxyl radical (OH^\bullet) would be generated on the surface of photocatalysts under simulated solar light illumination. Nitric oxide (NO) would be oxidized to nitrogen dioxide (NO_2), and finally oxidized to nitric acid (HNO_3) by these reactive oxygen species.



Scheme 1. Schematic illustration of the formation mechanisms for the hollow (a) and solid (b) TiO₂ microspheres during the aerosol-assisted flow synthesis process.

It is known that a larger band gap corresponds to more powerful redox ability [38]. Since BT has a larger band gap than PT, its oxidizing ability should be stronger. The oxidation reaction of NO in our experiment was believed to be initiated by $\cdot\text{OH}$ radicals. During the photocatalytic process, electron–hole carrier pairs will be generated under the illumination of light. These free delocalized charge carriers migrate to the catalyst surface and get trapped or annihilated through recombination. Because the charge transfer and recombination are two competitive reaction pathways, thus it is important to suppress the recombination rate and accelerate charge transfer in order to enhance the photocatalytic activity. From the results of XRD, SEM and N₂ sorption characterizations, we found that both the crystalline size and surface area of the resulting sample increased with the doping of boron into TiO₂. In most cases, higher crystallinity of titania leads higher photoactivity because the bulk recombination is effectively suppressed by reducing the bulk defects. These defects consume photoexcited electrons and act a recombination center [37]. Therefore, higher crystallinity is an important reason for the enhancement of photocatalytic activity of BT in comparison with undoped TiO₂ microspheres (PT). Meanwhile, large surface area of BT provides more surface sites for the adsorption of reactants molecules, making the photocatalytic process more efficient [41]. Additionally, the hollow structure may facilitate the harvesting of solar light and makes the transportation of NO through the interior space feasibly.

For the two Ni-doped TiO₂ samples, the existence of NiO can facilitate the excited electron transfer and hence efficiently suppress the recombination of photoproducted electron–hole [42]. This could enhance the photocatalytic activity of the Ni doped TiO₂ samples. From the characterization wavelength results of UV–vis DRS, it can be seen that the absorption wavelength range of the Ni-doped TiO₂ is extended greatly towards visible light, in comparison with undoped and B-doped TiO₂ photocatalyst, and its absorption intensity is also increased greatly. This can result in enhancing the generation of electron–hole pairs on the surface of Ni-doped TiO₂ catalysts. Therefore, we believe that a synergistic effect of boron and nickel dopants contributes to the highest photocatalytic activity of the B–Ni-codoped TiO₂ sample among the four products.

3.8. Formation mechanisms of hollow and solid TiO₂ microspheres

We propose possible mechanisms for the formation of hollow structured (BNT and BT) and solid (PT and NT) microspheres from the aerosol-assisted flow synthesis method (Scheme 1). The aerosol-assisted flow synthesis process began with homogeneous aqueous solution containing soluble precursors. When the droplets were sprayed into the tube furnace under high temperature (600 °C), the temperature decreased from the outer layer to the interior layer of the droplets. Consequently, the precursor ions

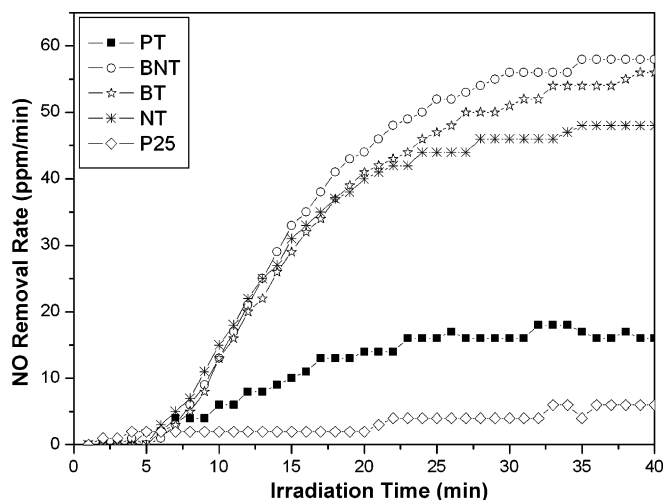


Fig. 7. Photocatalytic NO removal with the as-prepared samples under simulated solar light irradiation (residence time = 3.72 min, humidity levels = 2200 ppmv, and initial concentration of NO = 400 ppb).

(Ti⁴⁺, [B(OH)₄][−], Cl[−] and H⁺ ions) would gradually assemble in the interior layer of the droplets via the diffusion process and the solvent evaporation would happen simultaneously. Then the hydrolysis of TiCl₄ and the H₃BO₃ decomposition would proceed under the pyrolysis condition. H₃BO₃ would decompose into HBO₂ which is volatile at 600 °C. The HBO₂ gas emission is crucial for the formation of hollow structured particles (Scheme 1a). The main chemical reactions are proposed as follows:



As displayed in Fig. 2, hollow structured sample only existed when the precursor solution contained H₃BO₃. There was not H₃BO₃ in the precursor solution for the syntheses of the PT and NT samples, so they did not possess the hollow structure (Scheme 1b).

4. Conclusions

In this study, highly effective B-doped, Ni-doped and B–Ni-codoped TiO₂ microspheres photocatalysts were directly synthesized via an aerosol-assisted flow synthesis method. The addition of boron dopant resulted in hollow microspheres in both B-doped and B–Ni-codoped TiO₂ photocatalysts. The appearance of hollow structures could be ascribed to the escape of gas phase HBO₂ from the interior part of the TiO₂ microspheres during the pyrolysis reaction. All the doped TiO₂ microspheres exhibited enhanced photocatalytic activity than the undoped counterparts and the B–

Ni-codoped TiO₂ photocatalyst possessed superior photocatalytic activity to the as-prepared B- and Ni-doped TiO₂ products. The enhanced photocatalytic activity was explained and the formation mechanisms of hollow and solid microspherical structures were also proposed. We think this general method may be easily scaled up for industrial production of hollow and solid microspherical photocatalysts for NO removal under simulated solar light irradiation.

Acknowledgements

This work was supported by National Basic Research Program of China (973 Program) (Grant 2007CB613301), National Science Foundation of China (Grants 20673041, 20503009 and 20777026), Program for New Century Excellent Talents in University (Grant NCET-07-0352), the Key Project of Ministry of Education of China (Grant 108097), the Research Grants Council of Hong Kong (PolyU 5204/07E) and Hong Kong Polytechnic University (GYF08 and GYX75).

References

- [1] S.C. Lee, B. Wang, *Atmos. Environ.* 38 (2004) 941.
- [2] C.H. Ao, S.C. Lee, C.L. Mak, L.Y. Chan, *Appl. Catal. B: Environ.* 42 (2003) 119.
- [3] C.H. Ao, S.C. Lee, *Appl. Catal. B: Environ.* 44 (2003) 191.
- [4] C.H. Ao, S.C. Lee, S.C. Zou, C.L. Mak, *Appl. Catal. B: Environ.* 49 (2004) 187.
- [5] S.K. Joung, T. Amemiya, M. Murabayashi, K. Itoh, *Chem. Eur. J.* 12 (2006) 5526.
- [6] R. Asahi, T. Morikawa, T. Ohwaki, K. Aoki, Y. Taga, *Science* 293 (2001) 296.
- [7] S.U.M. Khan, M. Al-Shahry, W.B. Ingler Jr., *Science* 297 (2002) 2243.
- [8] S. Sakthivel, M. Janczarek, H. Kisch, *J. Phys. Chem. B* 108 (2004) 19384.
- [9] E.A. Reyes-Garcia, Y. Sun, K. Reyes-Gil, D. Raftery, *J. Phys. Chem. C* 111 (2007) 2738.
- [10] S. Sakthivel, H. Kisch, *Angew. Chem. Int. Ed.* 42 (2003) 4908.
- [11] J.H. Park, S.W. Kim, A.J. Bard, *Nano Lett.* 6 (2006) 24.
- [12] T. Tachikawa, S. Tojo, K. Kawai, M. Endo, M. Fujitsuka, T. Ohno, K. Nishijima, Z. Miyamoto, T. Majima, *J. Phys. Chem. B* 108 (2004) 19299.
- [13] J.C. Yu, W. Ho, J. Yu, H. Yip, P.K. Wong, J. Zhao, *Environ. Sci. Technol.* 39 (2005) 1175.
- [14] J.C. Yu, L. Zhang, Z. Zheng, J. Zhao, *Chem. Mater.* 15 (2003) 2280.
- [15] L. Lin, W. Lin, Y. Zhu, B. Zhao, Y. Xie, *Chem. Lett.* 34 (2005) 284.
- [16] D. Li, H. Haneda, S. Hishita, N. Ohashi, *Chem. Mater.* 17 (2005) 2588.
- [17] X. Hong, Z. Wang, W. Cai, F. Lu, J. Zhang, Y. Yang, N. Ma, Y. Liu, *Chem. Mater.* 17 (2005) 1548.
- [18] G. Liu, Z. Chen, C. Dong, Y. Zhao, F. Li, G.Q. Lu, H.-M. Cheng, *J. Phys. Chem. B* 110 (2006) 20823.
- [19] W. Zhao, W. Ma, C. Chen, J. Zhao, Z. Shuai, *J. Am. Chem. Soc.* 126 (2004) 4782.
- [20] I.E. Grey, C. Li, C.M. MacRae, L.A. Bursill, *J. Solid State Chem.* 127 (1996) 240.
- [21] K.Y. Jung, S.B. Park, S.K. Ihm, *Appl. Catal. B: Environ.* 51 (2004) 239.
- [22] S. In, A. Orlov, R. Berg, F. Garcia, S. Pedrosa-Jimenez, M.S. Tikhov, D.S. Wright, R.M. Lambert, *J. Am. Chem. Soc.* 129 (2007) 13790.
- [23] G. Liu, Y. Zhao, C. Sun, F. Li, G.Q. Lu, H.-M. Cheng, *Angew. Chem. Int. Ed.* 47 (2008) 4516.
- [24] D. Chen, D. Yang, Q. Wang, Z. Jiang, *Ind. Eng. Chem. Res.* 45 (2006) 4110.
- [25] T. Kasuga, M. Hiramatsu, A. Hoson, T. Sekino, K. Niihara, *Langmuir* 14 (1998) 3160.
- [26] B.D. Yao, Y.F. Chan, X.Y. Zhang, W.F. Zhang, Z.Y. Yang, N. Wang, *Appl. Phys. Lett.* 82 (2003) 281.
- [27] Z.Y. Liu, D.D. Sun, P. Guo, J.O. Leckie, *Chem. Eur. J.* 13 (2007) 1851.
- [28] H.G. Yang, H.C. Zeng, *J. Phys. Chem. B* 108 (2004) 3492.
- [29] R.A. Caruso, J.H. Schattka, A. Greiner, *Adv. Mater.* 13 (2001) 1577.
- [30] X.J. Cheng, M. Chen, L.M. Wu, G.X. Gu, *Langmuir* 22 (2006) 3858.
- [31] F. Caruso, X. Shi, R.A. Caruso, A. Susha, *Adv. Mater.* 13 (2001) 740.
- [32] Y. Lu, H. Fan, A. Stump, T.L. Ward, T. Rieker, C.J. Brinker, *Nature* 398 (1999) 223.
- [33] X. Jiang, C.J. Brinker, *J. Am. Chem. Soc.* 128 (2006) 4512.
- [34] Y. Huang, Z. Zheng, Z.H. Ai, L.Z. Zhang, X.X. Fan, Z.G. Zou, *J. Phys. Chem. B* 110 (2006) 19323.
- [35] S.D. Sharma, D. Singh, K.K. Saini, C. Kant, V. Sharma, S.C. Jain, C.P. Sharma, *Appl. Catal. A: Gen.* 314 (2006) 40.
- [36] K.S.W. Sing, D.H. Everett, R.A.W. Haul, L. Moscou, R.A. Pierotti, J. Rouquerol, T. Siemieniowska, *Pure Appl. Chem.* 57 (1985) 603.
- [37] K.Y. Jung, S.B. Park, *Appl. Catal. B: Environ.* 25 (2000) 249.
- [38] J. Lin, J.C. Yu, D. Lo, S.K. Lam, *J. Catal.* 183 (1999) 368.
- [39] G. Ertl, R. Hierl, H. Knozinger, N. Thiele, H.P. Urbach, *Appl. Surf. Sci.* 5 (1980) 49.
- [40] Y. Huang, W.K. Ho, S.C. Lee, L.Z. Zhang, G.S. Li, J.C. Yu, *Langmuir* 24 (2008) 3510.
- [41] X.C. Wang, J.C. Yu, Y.L. Chen, L. Wu, X.Z. Fu, *Environ. Sci. Technol.* 40 (2006) 2369.
- [42] Z.G. Zou, J.H. Ye, K. Sayama, H. Arakawa, *Nature* 414 (2001) 625.